

Modeling of deformation and failure behavior of dissimilar resistance spot welded joints under shear, axial and combined loading conditions

Sebastian Burget^{1,*}, Silke Sommer¹

¹ Crash-Safety, Damage Mechanics, Fraunhofer-Institute for Mechanics of Materials IWM, 79108 Freiburg, Germany

* Corresponding author: Sebastian.Burget@iwmm.fraunhofer.de

Abstract This paper presents the modeling of deformation and failure behavior of dissimilar resistance spot welded joints (RSW) between hot-stamped ultra-high strength (22MnB5) and microalloyed (HC340LAD) steels. To determine the deformation and failure behavior of the different material zones of the weld, tensile and shear specimens, which were cut from the base metals, the weld nugget and heat treated sheets were tested and modeled using the Gologanu-Leblond model coupled with the fracture criteria of Thomason and Embury. The joints were modeled using detailed 3-dimensional finite element models taking into account the different weld zones, i.e. base metal (BM), heat affected zones (HAZ) and weld metal (WM), their dimensions and their mechanical properties. Simulations of the spot welded joints' behavior under shear, axial and combined axial and shear loading were carried out and compared to experimental results such as force vs. displacement curves, load bearing capacities, fracture mode and fracture locations. Maximum loads and force vs. displacement curves from experiments and simulations showed good agreements for all loading situations examined. Despite of its superior strength compared to the microalloyed steel, pull-out fracture of the joints took place in the coarse grain HAZ of the hot-stamped ultra-high strength steel in experiments and simulations.

Keywords Resistance spot welding, Mechanical properties, Combined loading, Failure criterion, Ultra-high strength steel

1. Introduction

With several thousands of spot welds in a body-in-white, spot welding still represents the most widely used thermal joining process in steel-based automotive production. With the development of hot-stamped ultra-high strength steels, new light-weight potentials have been created, that combine thin steel sheets and thereby reduce weight, with a simultaneous optimization of passive safety requirements. To implement these potentials joining technologies have been adapted to ensure a combination of optimized material and joint strength. At present hot-stamped manganese-boron steels (22MnB5) are widely used, especially for load-bearing structural components in parts of the passenger cabin, where deformation and intrusion should be kept at a minimum.

To increase the reliability and accuracy of crash-simulations failure of the joints has to be taken into account using simplified models like solid or beam elements [1][2][3] in combination with simplified mostly force based failure criteria depending on the occurring axial and shear loads acting on the joints. To identify the model parameters of such criteria, failure of the joints can be characterized experimentally under different loading situations, as e.g. shown in [4][5]. For different welding parameters, which lead to a change in the joints' geometry in terms of different diameters of the weld nugget and the heat-affected zone [6], the procedure has to be repeated to determine the load bearing capacities of each particular joint.

In this work the deformation, fracture and load bearing capacity of dissimilar spot welds between hot-stamped and microalloyed steels is investigated in detailed finite-element simulations in several loading situations such as pure shear and pure axial loading as well as combined axial and shear loading. Material data for the modeling of the different material zones of the weld were obtained in tensile, notched tensile and double notched shear tests. The material models calibrated based on these tests are used for the simulation of experiments on spot-welded tensile-shear, KS2- and coach-peel specimens.

2. Experimental results

2.1. Dissimilar spot welded joints between ultra-high strength and low-alloyed steels

The joints investigated in this work are dissimilar resistance spot welded joints between a hot-stamped ultra-high strength steel (22MnB5) with a nominal ultimate tensile strength (UTS) of 1500 MPa and a microalloyed high strength low-alloy steel (HC340LAD) with an UTS of 415 MPa. Spot welding and testing of spot welded KS2-specimens was carried out at the Laboratory for Materials and Joining Technology (LWF) at the University of Paderborn [7].

On the left Fig. (1) shows the etched cross section of the dissimilar joint. The upper sheet shows the microalloyed HC340LAD with a sheet thickness of 1.5 mm. The hot-stamped 22MnB5 steel sheet with a thickness of 1.0 mm can be seen as the lower sheet in Fig. (1) (left). The averaged weld nugget diameter measured from cross-sections of three different spot welds was 5.2 mm.

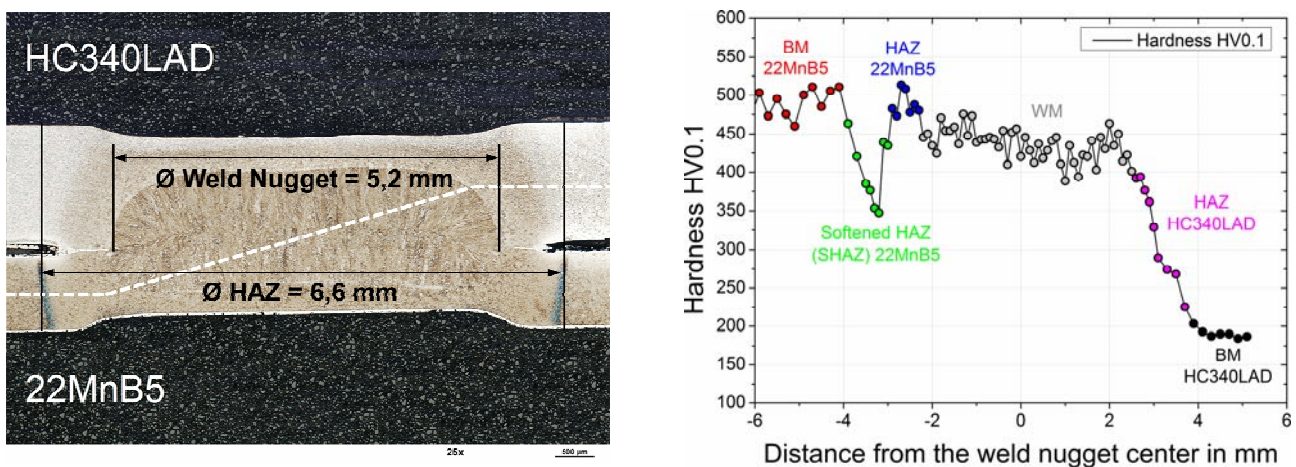


Figure 1. Etched cross section (left) and hardness measurements along the dashed white line shown in the cross section of the investigated spot welded joint between hot-stamped 22MnB5 and HC340LAD (right)

The base metal (BM) of the microalloyed steel shows a ferritic-perlitic microstructure with a hardness of 190HV0.1. Inside its HAZ the microstructure is ferritic-bainitic and a continuous increase in hardness up to 380HV0.1 adjacent to the weld nugget can be observed. The microstructures of the BM and the HAZ of the hot-stamped 22MnB5 are fully martensitic with averaged hardness values of 475HV0.1. Inside the subcritical HAZ a significant decrease in hardness can be seen. Due to the heat input during spot welding tempering of the martensitic microstructure occurs in this region (SHAZ) and leads to softening of the material. This phenomenon has also been observed during spot or laser welding of dual-phase steels as e.g. shown in [8]. The microstructure of the weld metal (WM) of the dissimilar weld is martensitic and has slightly lower hardness values than the BM and the HAZ of the hot-stamped manganese-boron steel.

2.2. Testing of dissimilar spot welded joints

The mechanical behavior of the dissimilar spot welded joints was characterized under shear, axial and combined axial and shear loading conditions using different tests and specimens such as tensile-shear- (TS), LWF-KS2- and coach-peel (CP) specimens. The LWF-KS2 concept [9] is based on double-U formed specimens, which are spot welded in their center and tested under different loading angles and/or velocities using different clamping conditions. The CP- and the KS2-specimen as well as the fixtures of the KS2-specimen for tests with different loading angles

are shown in Fig. (2). By using a pin-joint connecting the grips with the specimens fixtures no additional constraining forces arise during loading and only the applied vertical force acts on the joint.

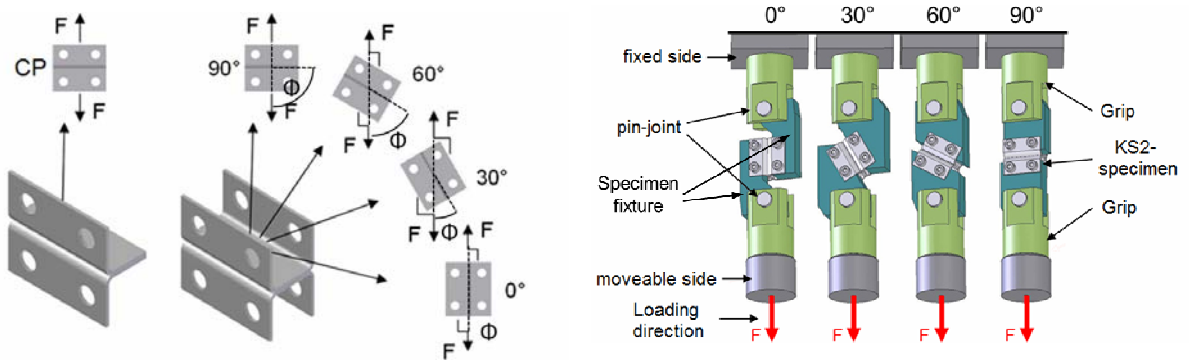


Figure 2. Coach-peel and KS2-specimens with loading angles 0°, 30°, 60° and 90° (left). Clamping conditions for the KS2-specimens tested under different loading angles (right) [9]

Assuming constant loading angles Φ , defined as the angle between the joining plane and the loading direction during deformation of the specimens, the measured forces F in KS2-experiments can be decomposed into their axial F_N and shear F_S parts as

$$F_N = F \cdot \sin \phi, \quad F_S = F \cdot \cos \phi. \quad (1)$$

Based on this decomposition simplified force-based failure criteria for spot welded joints as proposed by several authors [4][10][11] can be constructed. Fig. (3) (left) shows the force vs. displacement curves of all the KS2-experiments carried out on the investigated dissimilar spot welded joint. The decomposition of their load bearing capacities assuming constant loading angles is shown on the right. The gray dashed circular lines in Fig. (3) (right) indicate lines of constant resulting forces. The highest maximum load of the joint was measured under shear loading conditions in experiments on KS2-0° specimens. With increasing loading angles the load bearing capacity of the joint decreases to a minimum of 4.2 kN under pure axial loading in KS2-90° tests. Fracture of all tested specimens occurred as pull-out fracture from the hot-stamped 22MnB5 sheets. Cross-sections of failed specimens, loading capacities and results of TS- and CP-specimens will be shown in section 3.3.

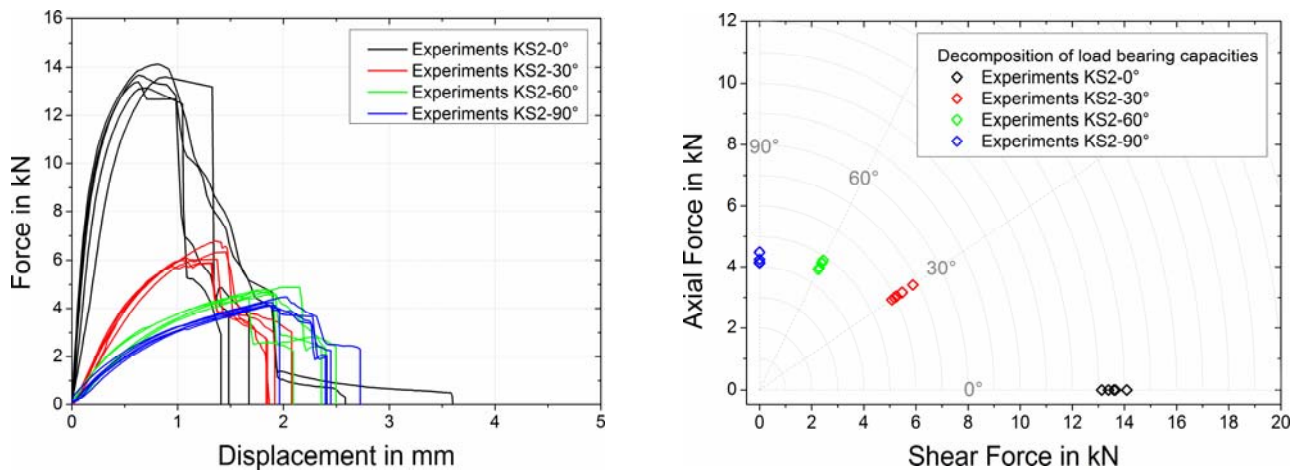


Figure 3. Force vs. displacement curves of KS2-specimens with loading angles 0°, 30°, 60° and 90° (left). Decomposition of load bearing capacities of the KS2 experiments into axial and shear forces (right)

3. Modeling of deformation and failure behavior of dissimilar spot welded joints

3.1. Material model

The constitutive model developed by Gologanu and Leblond [12] for porous media is an extension of the Gurson model [13] which takes into account the effect of void shape. In addition to the porosity f , the void shape S or w is considered in the flow potential of the model. Considering an oblate or prolate axisymmetric spheroidal void, shown in Fig. (4), with the semi-axes a along the x_2 - (axial direction) and b along the x_1 - and x_3 -direction (radial direction), w and the S are defined as $w=a/b$ and $S=\ln(a/b)=\ln(w)$. Spherical voids are characterized by $S = 0$ and $w = 1$ respectively. The shape parameters for prolate voids are $S > 0$ and $w > 1$, while $S < 0$ and $w < 1$ is true for oblate voids.

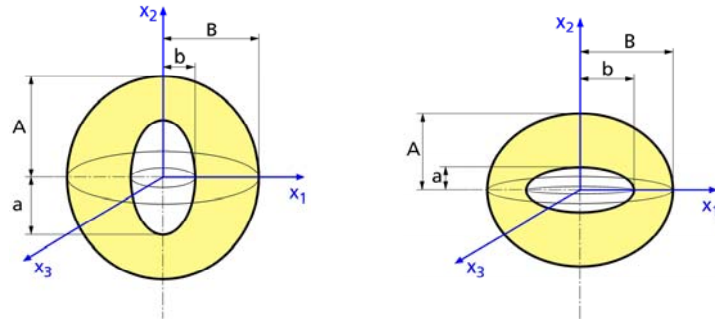


Figure 4. Spheroidal axisymmetric prolate (left) and oblate (right) void in a representative volume element with the shape of a confocal spheroid with the semi-axis A along x_2 and B along x_1 and x_3

The porosity of the representative volume element is given by

$$f = \frac{ab^2}{AB^2}. \quad (2)$$

The functional form of the flow potential, which was derived by Gologanu using an approximate load limit-analysis, is given in Eq. (3).

$$\Phi = C \frac{\|T_{ij}\|^2}{\sigma_M^2} + 2q_1(g+1)(g+f) \cosh\left(\frac{\kappa\Sigma_h}{\sigma_M}\right) - (g+1)^2 - q_1^2(g+f)^2 = 0 \quad (3)$$

with

$$\|T_{ij}\| = \sqrt{\frac{3}{2}T_{ij}T_{ij}} \quad (4)$$

T_{ij} and Σ_h are anisotropic generalizations of the deviatoric and the hydrostatic stresses. σ_M is the equivalent yield stress of the matrix material. The parameters C , q_1 , g and κ are functions of the void volume fraction f and the void shape S . The evolution of the void shape \mathcal{S} and the porosity in terms of the rate of void growth \mathcal{f}_{growth} and nucleation \mathcal{f}_{nuc} are given in Eq. (5) and Eq. (6) – (8).

$$\mathcal{S} = S_a \mathcal{E}'_a + S_b \mathcal{E}'_{kk} \quad (5)$$

The parameters S_a and S_b are functions of the void shape and the stress triaxility. \mathcal{E}'_a and \mathcal{E}'_{kk} are the deviatoric part of the plastic strain rate in the direction of the semi-axis a and the rate of

volumetric strain. Compared to the Gurson model, no modifications are needed to describe the evolution of porosity. The rate of f consists of two terms describing growth and nucleation of voids.

$$\dot{f} = \dot{f}_{growth} + \dot{f}_{nuc} \quad (6)$$

Void growth is governed by the rate of volumetric plastic strain, whereas void nucleation is assumed to be controlled by the equivalent plastic strain $\varepsilon_{pl,M}$ of the matrix material. Under the assumption that void nucleation follows a normal distribution, its rate is given by Eq. (8).

$$\dot{f}_{growth} = (1-f)\dot{\varepsilon}_{kk}^p \quad (7)$$

$$\dot{f}_{nuc} = \frac{f_n}{S_N \sqrt{2\pi}} \exp\left(-\frac{1}{2}\left(\frac{\varepsilon_{pl,M} - \varepsilon_N}{S_N}\right)^2\right) \dot{\varepsilon}_{pl,M} \quad (8)$$

f_n denotes the overall volume fraction of void nucleating inclusions, ε_N is the mean value of the equivalent plastic strain, at which inclusions nucleate voids and S_N is the standard deviation of the normal distribution.

Together with the Gologanu model the fracture criteria of Thomason [14], in a modified version of Pardoen and Hutchinson [15], and Brown and Embury [16] are used. The Thomason model assumes that void coalescence begins once the plastic limit load on the ligament between the voids is reached. The limit load is derived using an axisymmetric unit-cell containing one ellipsoidal void of a regular array shown in Fig. (5).

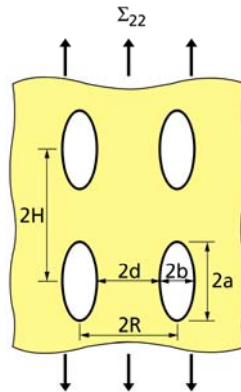


Figure 5. Geometrical quantities of the void distribution used for the Thomason model

The coalescence criterion is then expressed by Eq. (9), where α and β are material parameters. Unit cell analyses suggest to choose $\alpha = 0.1$ and $\beta = 1.2$ [15]. Based on the geometry the ligament size ratio can be written as Eq. (10).

$$C_{Thomason} = \frac{\Sigma_{22}}{\sigma_M} - \left(1 - \left(\frac{b}{R}\right)^2\right) \left(\alpha \left(\frac{R/b-1}{w}\right)^2 + \beta \left(\frac{R}{b}\right)^{1/2} \right) = 0 \quad (9)$$

$$\frac{b}{R} = \left[\frac{3}{2} \frac{f}{w} \frac{H_0}{R_0} \exp\left(\frac{3}{2} \varepsilon'_{22}\right) \right]^{1/3} \quad (10)$$

The Gologanu model calculates f , w , Σ_{22} and σ_M in Eq. (9) and (10). The initial aspect ratio H_0/R_0 can be considered, besides α and β , as a third material parameter of the failure criterion.

To model material failure at low stress triaxilities, the criterion of Brown and Embury [16] is used here. This model is based on the assumption that the formation of shear bands takes place in the ligament between two voids and leads to ductile fracture, if the mean radius of a void equals half the distance between the centers of the two voids. Using the void aspect ratio w , calculated by the

Gologanu model, this criterion can be written as

$$C_{Embury} = \sqrt{1 + w^2} - \frac{R}{b} = 0. \quad (11)$$

The model has been implemented by Andrieux [17] into the finite element code ABAQUS/Explicit.

3.2. Identification of model parameters of the different weld zones

The parameters of the Gologanu model and the fracture criteria were identified by inverse simulations of smooth and notched tensile specimens as well as double notched shear specimen, which were cut from the base materials, the weld nugget itself and heat treated sheets with microstructures corresponding to the heat affected zones. In case of the specimens cut from the weld nugget reduced dimensions have had to be used, due to the geometry of the weld nuggets. All specimens have been modeled using detailed finite element models meshed with 3-dimensional brick elements with edge lengths of 0.1 mm in the regions of interest. Using the symmetry of the specimens only one eighth of the smooth and notched tensile specimen and half of the double notched shear specimen has been modeled. The finite element models are shown in Fig. (6).

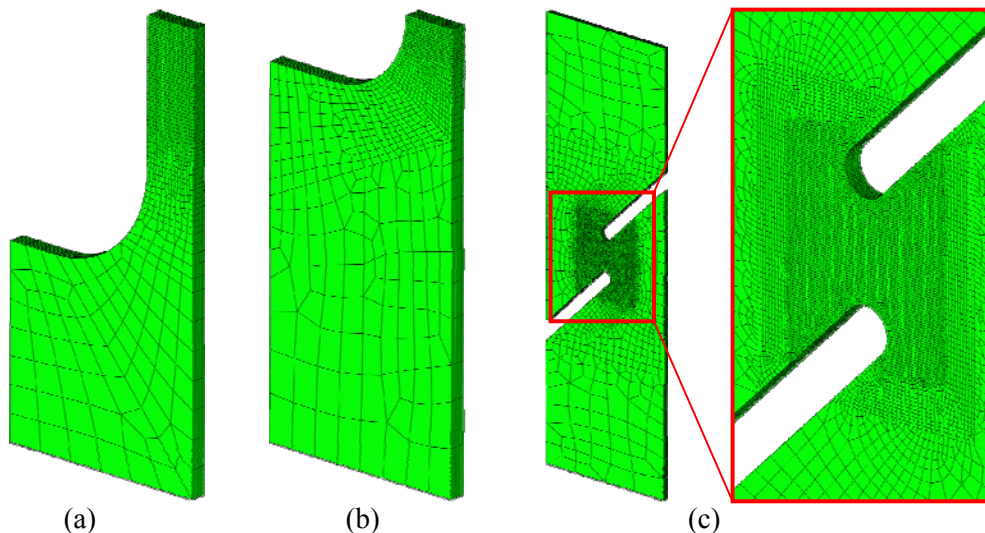


Figure 6. Finite element models of smooth (a) and notched tensile (b) and double notched shear (c) specimens

Up to uniform elongation the true stress-strain curves of the base material, heat affected zones and the weld metal were measured in smooth tensile tests. Subsequently the true stress vs. true strain curves are determined in simulations of the smooth tensile tests. The damage and failure parameters for the different material zones of the weld were identified by simulating the smooth and notched tensile tests and the shear tests on double notched shear specimens and adjusting the parameters to match the numerical results with the experimental ones. The parameters identified are given in Table (1).

Table 1. Parameters of the material model and the failure criteria

	f_0	ε_N	f_N	S_N	q	S_0	H_0/R_0	α	β
22MnB5 BM	0.002	0.20	0.02	0.1	1.5	0.0001	1.2	0.1	1.2
22MnB5 SHAZ	0.002	0.30	0.008	0.1	1.5	0.0001	1.2	0.1	1.2
HC340LAD BM	0.002	0.85	0.003	0.1	1.5	0.0001	0.5	0.1	1.2
HC340LAD HAZ	0.002	0.15	0.005	0.1	1.5	0.0001	0.5	0.1	1.2
WM	0.002	0.15	0.02	0.1	1.5	0.0001	1.8	0.1	1.2

The comparison of experimental and numerical results for the 5 different material zones is shown in Fig (7) – Fig. (9). The simulation results show good agreements with the experimental measurements for all loading conditions and stress triaxilities. It should be noted that the specimens for the characterization of the weld metal and the smooth tensile specimens from the HAZ of HC340LAD have been manufactured and tested with reduced dimensions and gauge lengths to obtain valid experimental data. The materials' ductility in terms of technical fracture strains in tensile tests cannot be compared in these cases.

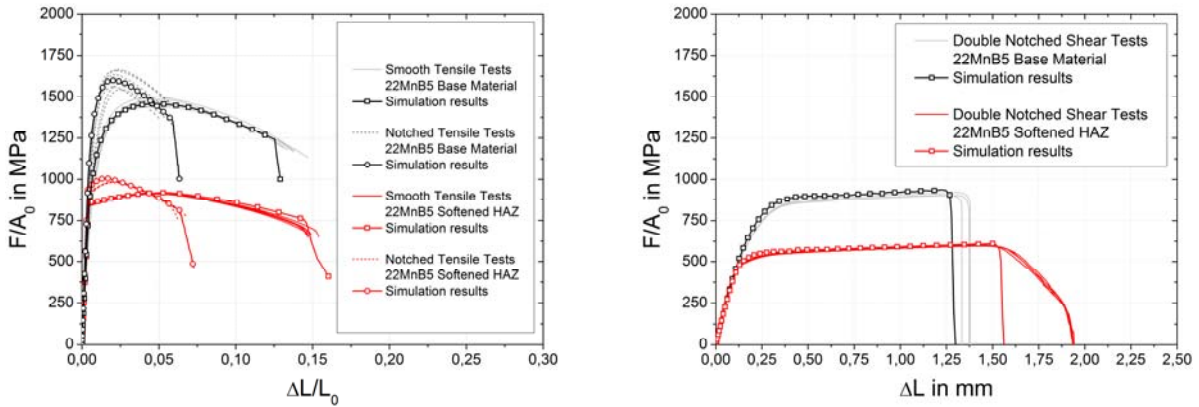


Figure 7. Comparison of measured and calculated F/A_0 vs. $\Delta L/L_0$ curves of smooth and notched tensile tests (left) and F/A_0 vs. ΔL curves of double notched shear tests (right) for 22MnB5 (BM and softened HAZ)

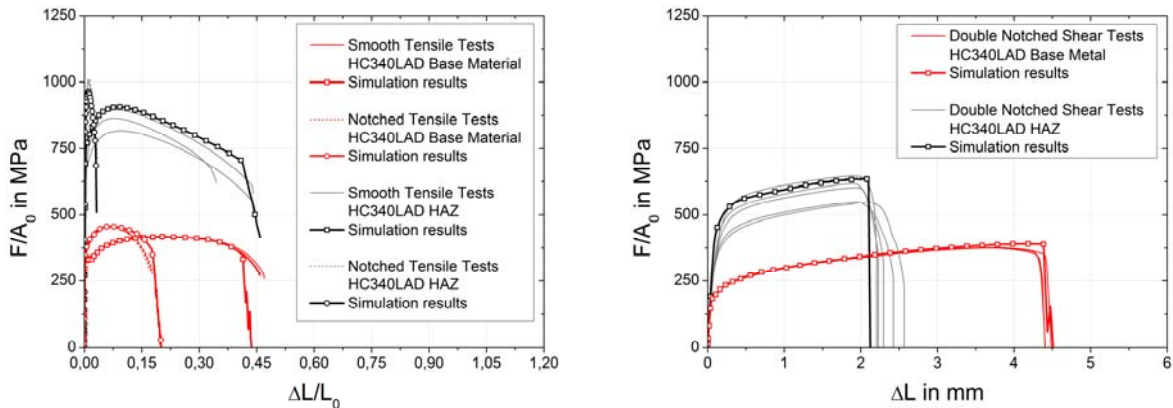


Figure 8. Comparison of measured and calculated F/A_0 vs. $\Delta L/L_0$ curves of smooth and notched tensile tests (left) and F/A_0 vs. ΔL curves of double notched shear tests (right) for HC340LAD (BM and HAZ)

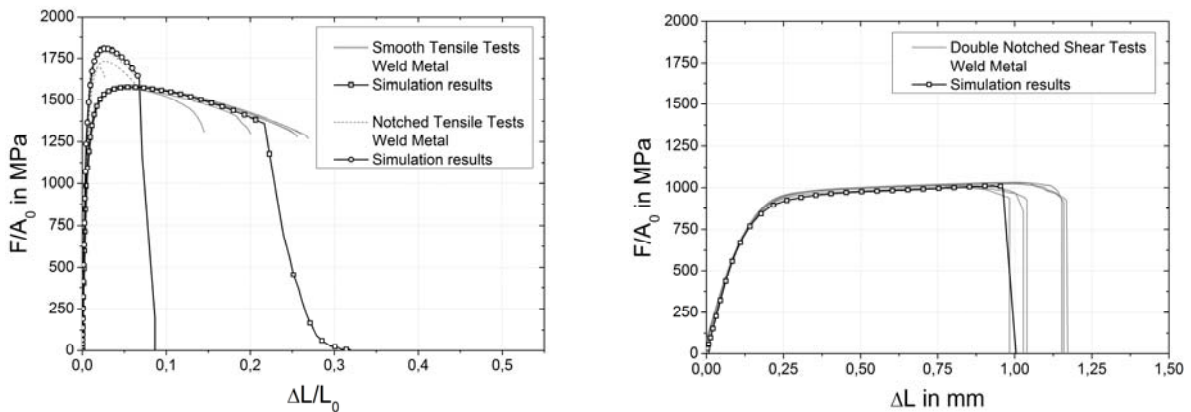


Figure 9. Comparison of measured and calculated F/A_0 vs. $\Delta L/L_0$ curves of smooth and notched tensile tests (left) and F/A_0 vs. ΔL curves of double notched shear tests (right) for the WM

3.3. Simulation of tensile-shear-, KS2- and coach-peel tests

For the simulation of deformation and failure behavior of dissimilar spot welded joints in tensile-shear- (TS), KS2- and coach-peel (CP) tests, the calibrated material and failure models were used for the different material zones of the weld. Due to the negligible differences in the mechanical behavior between the base material of 22MnB5 and the weld metal as well as the similar hardness values of the base metal, the weld metal and the non-softened HAZ in 22MnB5, the mechanical properties of the non-softened HAZ were assumed to be identical to those of the weld metal. A detailed finite-element model of the spot weld, shown in Fig. (10), was built up taking into account the geometry of the weld and its material zones measured in etched cross-sections and hardness measurements of spot welded specimens (see Fig.(1)). The nugget diameter and the diameter of the HAZ of the spot weld were modeled as 5.2 mm and 6.6 mm respectively. The softened HAZ in the hot-stamped 22MnB5 sheet was modeled with a width of 0.6 mm. The edge length of the elements in the spot welded region is approximately 0.1 mm.



Figure 10. Detailed finite element model of the spot weld between 22MnB5 and HC340LAD

The finite-element models of TS-, KS2- and CP-specimens are shown in Fig. (11). Due to the symmetry only one half of each specimen was modeled. The parts of the specimens that are clamped in the experiments, shown in dark gray, are taken as rigid bodies. The grips and the specimen fixtures of the KS2-tests were not explicitly taken into account. Instead of that the clamping conditions of the specimens have been modeled by connecting all nodes of the clamped rigid bodies via kinematic constraints to one node representing the pin-joint between the specimen fixtures and the grips (see Fig. (2)). This is shown schematically in Fig. (11).

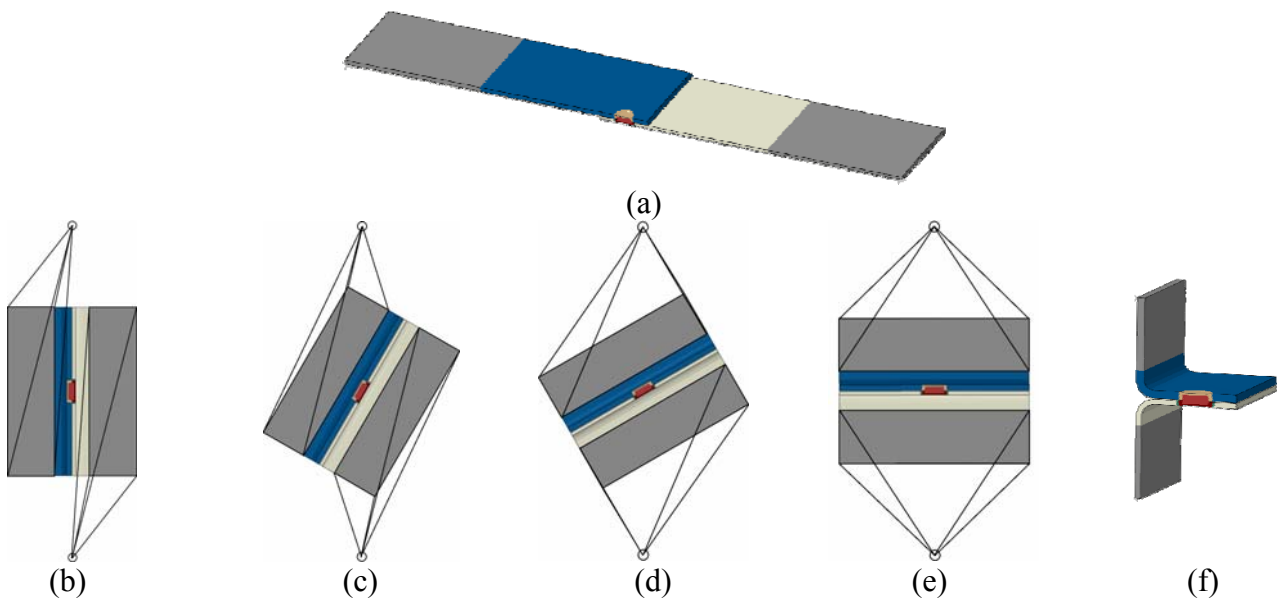


Figure 11. Detailed finite element models of the spot welded tensile-shear specimen (a), KS2-0° (b), -30° (c), -60° (d), -90° (e) specimens and the coach-peel specimen (f)

All simulations were performed using the finite element code ABAQUS/Explicit version 6.9. The calculated force vs. displacement curves for the six different loading situations of the spot welded joints are shown together with the corresponding experimental data in Fig. (12). The measured force vs. displacement curves of all specimens are reproduced well by the numerical results. Also the calculated and experimental load bearing capacities (see Table (2)) agree well.

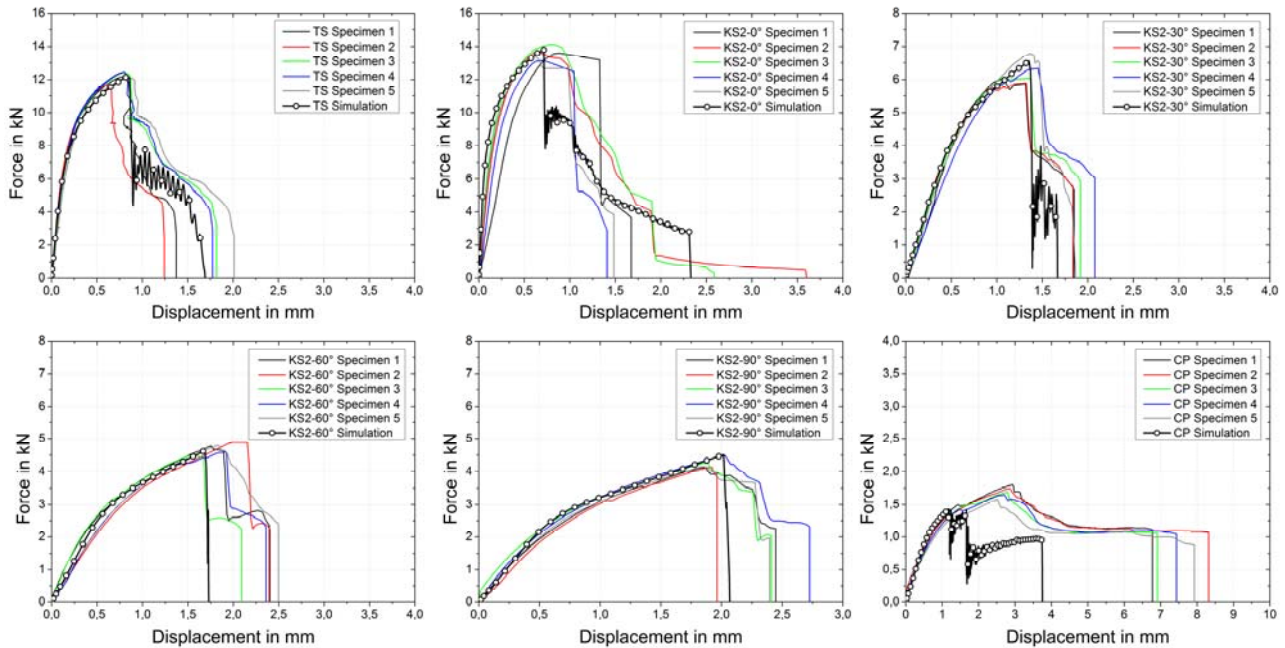


Figure 12. Comparison of measured and calculated force vs. displacement curves for tensile-shear-, KS2-0°, -30°, -60° and -90° and coach-peel specimens

Failure of the joints in shear tests, i.e. TS- and KS2-0° tests, is calculated as pull-out fracture inside the softened HAZ of the hot-stamped 22MnB5. During loading of both of the shear-specimens deformation localizes inside the SHAZ of 22MnB5 leading to pull-out fracture of the joint. Failure of the SHAZ occurs due to the Thomason criterion. The calculated fracture location was confirmed in observations of polished and etched cross-sections of the tested TS-specimens (see Fig. (13)).

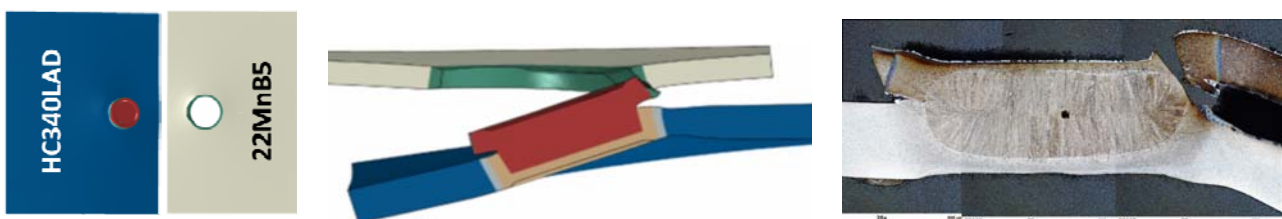


Figure 13. Calculated pull-out fracture of TS-specimen inside the softened HAZ of 22MnB5 (left and middle) Polished and etched cross-section of a tested TS-specimen showing pull-out fracture inside the SHAZ (right)

In pure axial loading situations in KS2-90° tests, pull-out fracture of the joints does not initiate inside the softened HAZ, but occurs inside the coarse grain HAZ of 22MnB5 directly adjacent to the weld nugget. The same fracture behavior is observed under combined loading conditions in KS2-30° and KS2-60° tests as well as in CP-tests. Fracture occurs in the ultra-high strength steel due to the lower sheet thickness and the lower ductility of its HAZ compared to that of the microalloyed steel. In all cases the critical criterion for failure initiation of the joints in simulations was found to be the Thomason criterion. As an example Fig. (14) shows the comparison between calculated and experimentally observed fracture appearance and locations for KS2-90° specimens.

Table 2. Comparison of measured and calculated load bearing capacities of the dissimilar joints

	TS	KS2-0°	KS2-30°	KS2-60°	KS2-90°	CP
$F_{\max,av}$ Exp.	12.16 kN	13.57 kN	6.20 kN	4.67 kN	4.20 kN	1.66 kN
F_{\max} Sim.	12.19 kN	13.78 kN	6.56 kN	4.64 kN	4.51 kN	1.43 kN
Deviation in %	+ 0,25	+ 1,55	+ 5,81	- 0,64	+ 7,38	-13,86

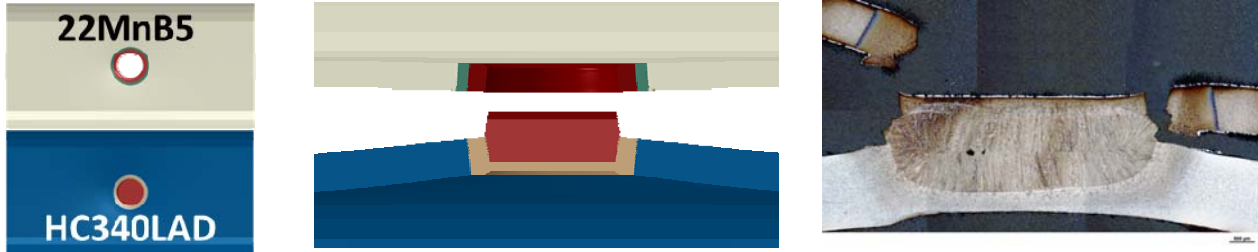


Figure 14. Calculated pull-out fracture of KS2-90° specimen (left and middle). Polished and etched cross-section of a tested KS2-90° specimen showing fracture inside the coarse grain HAZ of 22MnB5 (right)

Based on the simulations of TS- and KS2-specimens the applied loads were decomposed into axial and shear forces according to the current loading angles during deformation of the specimens as shown in Fig. (15). It can be seen that the loading angles of all specimens, except the KS2-90° specimen, which is loaded under pure axial forces, deviate from their original values due to rotation of the weld nuggets during deformation. In KS2-60° and KS2-30° tests only minor rotations of the weld occur. Therefore the deviation from their original loading angle is negligible. In this case the measured load bearing capacities from experiments could be directly decomposed into their components to be used as values for the adjustment or construction of force-based failure criteria. In shear loading conditions larger weld rotations were observed. Up to the maximum forces rotations of 12.2° and 9.6° were calculated for TS- and KS2-0° specimens respectively. Caused by the rotation the axial forces acting on the joints increase to 2.6 kN for TS- and 2.3 kN for KS2-0° specimens. The assumption of constant loading angles for the adjustment or the construction of simplified force based failure criteria should not be made in this case, but can be taken from numerical simulations.

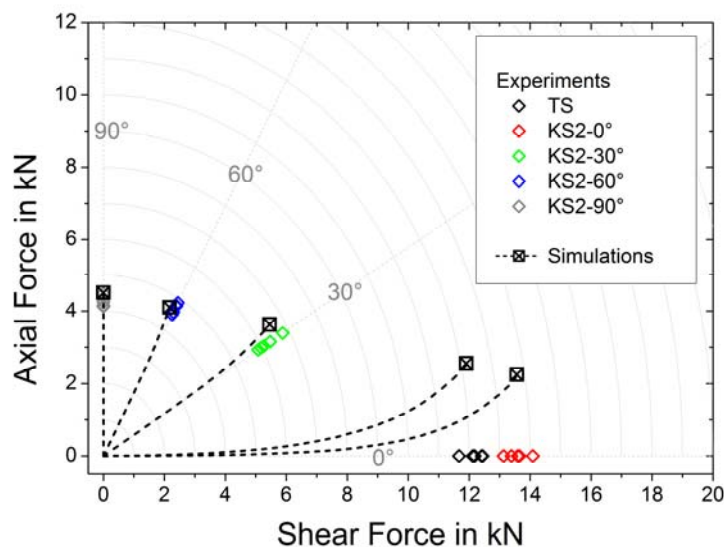


Figure 15. Decomposition of measured and calculated load bearing capacities into axial and shear forces acting on the joint. The evolution of axial and shear forces during deformation of the specimens in simulations are shown by the dashed black lines

4. Conclusion

Based on the calibrated Gologanu material models and failure criteria of Thomason and Brown and Embury for the different material zones of resistance spot welded joints between the hot-stamped ultra-high strength steel and the microalloyed HSLA steel, the joints' behavior in terms of force vs. displacement curves, load bearing capacities, fracture mode and fracture locations can be calculated using detailed finite-element models according to the joints geometry. In the cases investigated pull-out fracture of the joints under shear loading took place inside the softened HAZ of 22MnB5 due to localization of plastic deformation. Under combined axial and shear loading as well as under pure axial loading situations a change in fracture location can be observed. In these cases fracture occurred as pull-out fracture in the coarse grain HAZ of 22MnB5 directly adjacent to the weld nugget. Fracture initiation of all joints is calculated due to the Thomason criterion.

The evolution of axial and shear forces acting on the weld during different loading situations could be obtained by decomposing the applied loads into their axial and shear components according to their true loading angles. Such results can be used for the adjustment or the identification and construction of simplified force based failure criteria used for simplified spot weld models in crash simulations. Furthermore, factors influencing the load bearing capacity of the joints, as e.g. sheet thickness, weld nugget diameter or other geometrical quantities can be investigated by means of detailed finite-element modeling of spot welded joints between the investigated materials without further experimental effort.

Acknowledgements

The results presented are part of the research project P806/A262. The research project was conducted with professional supervision and financial support of the Research Association for Steel Application (FOSTA), Düsseldorf, Germany and the Research Association of the Working Group of the Iron- and Metal-processing Industry e.V. (AVIF), Ratingen, Germany by the Stiftung Stahlanwendungsforschung. Sincere thanks are given for the sponsorship.

References

- [1] LS-DYNA Keyword User's Manual, Version 971, Livermore Software Technology Corporation (LSTC), 2010.
- [2] PAM-CRASH/SAFE Solver Notes Manual, ESI Software GmbH, 2004.
- [3] ABAQUS Analysis user's manual, Version 6.9. Hibbit, Karlsson & Sorensen Inc., 2004.
- [4] J.H. Song, H. Huh, Failure characterization of spot welds under combined axial-shear loading conditions, *International Journal of Mechanical Sciences*, 53 (2011) 513 – 525.
- [5] S.-H. Lin, J. Pan, S.-R. Wu, T. Tyan, P. Wung, Failure loads of spot welds under combined opening and shear static loading conditions, *International Journal of Solids and Structures*, 39 (2002) 19 – 39.
- [6] S. Aslanlar, The effect of nucleus size on mechanical properties in electrical resistance spot welding of sheets used in automotive industry, *Materials & Design*, Vol. 27 (2006), 125 – 131.
- [7] S. Sommer, S. Burget, F. Klokke, D. Hein, D. Krätschmer, H.-J. Wink, Charakterisierung und Ersatzmodellierung des Bruchverhaltens von Punktschweißverbindungen aus ultrahochfesten Stählen für die Crashesimulation unter Berücksichtigung der Auswirkungen der Verbindung auf das Bauteilverhalten, Final report FOSTA/AVIF P806/A262, to be published
- [8] V.H. Baltazar Hernandez, S.K. Panda, M.L. Kuntz, Y. Zhou, Nanoindentation and microstructure analysis of resistance spot welded dual phase steel, *Material Letters*, 64 (2010), 207 – 210.
- [9] O. Hahn, D. Gieske, A. Rhode, Probe und Probenspannvorrichtung zum Einsatz in

Zugmaschinen, Patent specification DE 195 22 247 A1, 1996

- [10] S.-H Lin, J. Pan, T. Tyan, P.Prasad, A general failure criterion for spot welds under combined loading conditions, *International Journal of Solids and Structures*, 40 (2003), 5539 – 5564.
- [11] P. Wung, A force-based failure criterion for spot weld design, *Experimental Mechanics*, 41 (2001), 107 – 113.
- [12] G. Gologanu, J.B. Leblond, G. Perrin, J. Devaux, Recent Extensions of Gurson’s Model for Porous Ductile Metals, *Continuum Micromechanics*, CISM Courses and Lectures No. 377, ed. by P. Suquet, pp. 61-130, 1997.
- [13] A.L. Gurson, Continuum Theory of ductile rupture by void nucleation and growth Part I. Yield criteria and flow rules for porous ductile media, *J. of Eng. Materials and Technology*, 99 (1977), 2 – 15.
- [14] P.F. Thomason, *Ductile Fracture of Metals*, Pergamon Press, Oxford, 1990
- [15] T. Pardoen, J.W. Hutchinson, An extended model for void growth and coalescence, *J. Mech. Phys. Solids*, Vol.48 (2000) , 2467 – 2512.
- [16] L.M. Brown, J.D. Embury, Proc. 3rd Int. Conf. on Strength of Metals and Alloys, London Institute of Metals, 1973
- [17] F. Andrieux, D.-Z. Sun, H. Riedel, Troyes France, Proc. Int. Forum on Advanced Material Science and Technology IFAMST04 on CD, 2004